# NF−κB Binding Mechanism: A Nuclear Magnetic Resonance and Modeling Study of a GGG → CTC Mutation ‡

**ARTICLE** *in* BIOCHEMISTRY · APRIL 1999

Impact Factor: 3.02 · DOI: 10.1021/bi982402d · Source: PubMed



**3 AUTHORS**, INCLUDING:

Muriel Delepierre
Institut Pasteur International Network
**199** PUBLICATIONS **4,740** CITATIONS

SEE PROFILE

# NF-κB Binding Mechanism: A Nuclear Magnetic Resonance and Modeling Study of a GGG → CTC Mutation‡

Carine Tisné,§ Brigitte Hartmann,|| and Muriel Delepierre*,§

*Laboratoire de RMN, Institut Pasteur, CNRS URA 1129, 28 rue du Docteur Roux, 75015 Paris, France, and Laboratoire de Biochimie Théorique, Institut de Biologie Physico-Chimique, CNRS UPR 9080, 13 rue Pierre et Marie Curie, 75005 Paris, France*

*Received October 8, 1998; Revised Manuscript Received December 15, 1998*

ABSTRACT: We present the solution structure of the nonpalindromic 16 bp DNA 5′d(CTGCTCACTTTC-CAGG)3′. 5′d(CCTGGAAAGTGAGCAG)3′ containing a mutated κB site for which the mutation of a highly conserved GGG tract of the native κB HIV-1 site to CTC abolishes NF-κB binding. $^{1}$H and $^{31}$P NMR spectroscopies have been used together with molecular modeling to determine the fine structure of the duplex. NMR data show evidence for a BI−BII equilibrium of the CpA·TpG steps at the 3′-end of the oligomer. Models for the extreme conformations reached by the mutated duplex (denoted 16M) are proposed in agreement with the NMR data. Since the distribution of BII sites is changed in the mutated duplex compared to that of the native duplex (denoted 16N), large differences are induced in the intrinsic structural properties of both duplexes. In particular, in BII structures, 16M shows a kink located at the 3′-end of the duplex, and in contrast, 16N exhibits an intrinsic global curvature toward the major groove. Whereas 16N can reach a conformation very favorable for the interaction with NF-κB, 16M cannot mimic such a conformation and, moreover, its deeper and narrower major groove could hinder the DNA−protein interactions.

The rel/NF-κB transcription factors are expressed in most cell types. These proteins are involved in the regulation of many genes related to various functions such as immune and inflammatory responses and cellular growth and development. NF-κB is also subverted by a number of viruses, including HIV-1[1] (*1*−*3*), to activate the expression of viral genes. Five DNA−NF-κB crystal structures have been published (*4*−*8*). The three first structures involve a p50 or p52 homodimer bound to DNA. Two different binding modes of p50 are observed, although the DNA sequences only differ by one base pair. The fourth crystal structure involves a p50-p65 heterodimer bound to DNA. NF-κB(p50-p65) recognizes κB elements with a consensus sequence of 5′GGGRNYYY-CC3′ (R for purine, Y for pyrimidine, and N for any nucleotide). In the crystal structure (*7*), p50 contacts 5 bp at the 5′-end of DNA, whereas the subsite of p65 involves 4 bp at the 3′-end of the duplex. The last crystal structure is a p65 homodimer complexed with DNA (*8*). Overall, these X-ray studies showed that contacts with DNA occur in the major groove through loops connecting the various β-strands of Rel proteins. Furthermore, all Rel proteins make extensive contacts with the phosphate backbone of their cognate DNA. In most of these structures, the DNA helix axis exhibits a curvature toward the major groove in agreement with a previous circular mobility shift assay study carried out with the κB site of the HIV-1 (*9*).

Recently, we have determined the solution conformation of the 16 bp duplex containing the 10 bp of the HIV-1 κB site (*10*). We showed that NMR data were in agreement with an equilibrium between two different conformations, identified as a phosphodiester backbone movement at the two dinucleotide steps flanking the 10 bp binding site of NF-κB. More precisely, the two dihedral backbone angles ε and ζ change from the BI (t, g−) to the BII (g−, t) conformation. Molecular modeling and an appropriate refinement strategy allowed us to propose a model for each extreme conformation. One of these conformations exhibits a novel mode of intrinsic curvature toward the major groove consistent with the curvature of DNA observed in the X-ray p50-p50−DNA (*11*) and p50-p65−DNA (*7*) structures. Thus, we demonstrated that the isolated κB site has the potential to bend and that the intrinsic structural properties of DNA can suggest a mode of specific recognition.

Here, we present the solution structure of a mutated κB site (16M) where the mutation of the highly conserved GGG tract into CTC abolishes NF-κB binding (*1*). In the crystallographic p50-p65−DNA structure, six hydrogen bonds are observed within this guanine tract. The mutation changes two acceptor N7 atoms into two acceptor N4 or O4 atoms, and one O6 atom is conserved. Therefore, only three hydrogen bonds are abolished and the 3′-subsite where p65 binds remains intact. Moreover, as the p50-p65 heterodimer presents a particularly high DNA affinity, sources other than DNA readout seem to contribute. The extensive phosphate contacts could provide such an effect (*7*). Therefore, in the

‡ The structures of the native duplex have been deposited in the Brookhaven Protein Data Bank under identification codes 1kbd (for the BI family) and 2kbd (for the BII family), whereas the structures of the mutated duplex have been deposited under identification codes 3kbd (for the BI family) and 4kbd (for the BII family).

* To whom correspondence should be addressed.

§ CNRS URA 1129.

|| CNRS UPR 9080.

[1] Abbreviations: bp, base pair; HIV-1, human immunodeficiency virus type 1; NOE, nuclear Overhauser effect; rms, root-mean-square deviation.

10.1021/bi982402d CCC: $18.00 
Published on Web 03/11/1999

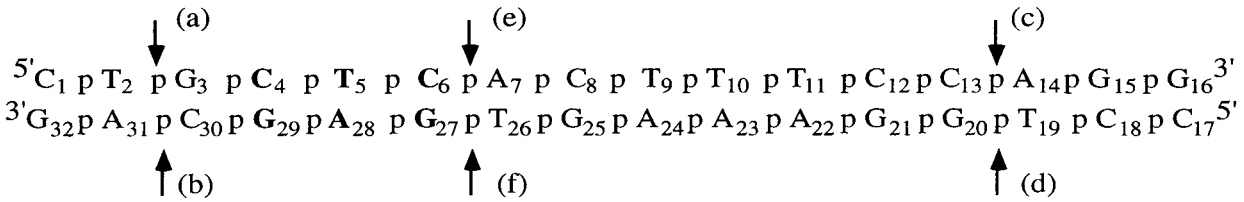


FIGURE 1: Sequence of the mutated duplex. The mutated bases are denoted in bold. Arrows indicate steps that exhibit unusual backbone flexibility. References to these steps in the text will be given using the letter in parentheses. For the purpose of clarity, **cd** structures will refer to a structure for which BII conformations have been generated at steps (c) and (d), and BI conformation for the other steps; **cde** structures will refer to the BII conformation at steps (c), (d), and (e) and the BI conformation for the other steps; and **e** structures will refer to the BII conformation at step (e) and the BI conformation for the other steps.

mutated $\kappa$B site, the hydrogen bond change seems to be insufficient to explain the lack of NF-$\kappa$B binding.

The aim of this work was to investigate by NMR spectroscopy and molecular modeling the structure and flexibility of the mutated sequence to determine which nucleotides are affected and to what extent. Compared to the native $\kappa$B site, $^{31}$P NMR data and NOE-derived distances from the mutated duplex show differences in the conformational equilibrium of the phosphodiester backbone and in several structural parameters, in particular the groove size. The modeling of 16M confirms these features and moreover reveals differences in helix curvature compared to 16N. This study also stresses the importance of sequence for BI−BII equilibria of the phosphodiester backbone, as already predicted by molecular modeling (*12*). Above all, these results establish that sequence context effects, both upstream and downstream of a DNA binding site, can thus play an important role in providing an effective protein binding site.

## MATERIALS AND METHODS

*Sample Preparation*. The 16 bp DNA duplex (16M) $^{5'}$d($C_1T_2G_3C_4T_5C_6A_7C_8T_9T_{10}T_{11}C_{12}C_{13}A_{14}G_{15}G_{16}$)$^{3'}$•$^{5'}$d($C_{17}C_{18}$-$T_{19}G_{20}G_{21}A_{22}A_{23}A_{24}G_{25}T_{26}G_{27}A_{28}G_{29}C_{30}A_{31}G_{32}$)$^{3'}$ was synthesized as previously described (*13*). The final concentration was approximately 6 mM, and the pH of the sample was adjusted to 7. The nomenclature used for 16M is described in the legend of Figure 1.

The sequence of the native $\kappa$B site (16N) previously studied (*10*) is $^{5'}$d($C_1T_2G_3G_4G_5G_6A_7C_8T_9T_{10}T_{11}C_{12}C_{13}A_{14}$-$G_{15}G_{16}$)$^{3'}$•$^{5'}$d($C_{17}C_{18}T_{19}G_{20}G_{21}A_{22}A_{23}A_{24}G_{25}T_{26}C_{27}C_{28}C_{29}C_{30}A_{31}G_{32}$)$^{3'}$.

*NMR Spectroscopy*. All NMR experiments were carried out on a Varian Unity spectrometer (11.7 T) operating at a proton frequency of 500 MHz. The spectrometer was equipped with a 5 mm indirect detection probe. The conformational analysis of both duplexes was carried out at 35 °C, a temperature at which the DNA is in a duplex form (*10*, *13*). Proton spectra in $^2H_2O$ are referred to external (trimethylsilyl)-3-propionic acid-2,2,3,3-$d_4$ sodium salt (TMSP). $^{31}$P chemical shifts are referred to external phosphoric acid (85%) at 0 ppm.

Assignments of nonexchangeable proton and of phosphorus resonances of 16M were carried out as described elsewhere (*13*). The labile proton resonances of 16M were assigned using the NOESY WATERGATE (*14*) experiment conducted at 25 °C to slow their exchange rate and with a mixing time of 150 ms. The experiment was acquired with 2048 data points in the $t_2$ dimension and 512 $t_1$ increments; 16 transients were collected per $t_1$ increment. The spectral width was 12 000 Hz in both dimensions. The selective 180° pulse was performed with a tailored excitation pulse train using 300 $\mu$s between each pulse of the composite pulse. The gradient duration was 1 ms for a gradient amplitude of 11 G/cm for the first gradient and 17 G/cm for the gradient echo.

For the quantitative analysis of NOE interactions, NOESY spectra were recorded successively at five different mixing times, namely, 70, 100, 150, 200, and 250 ms. These experiments were acquired with 2048 data points in the $t_2$ dimension and 470 $t_1$ increments; 48 transients were collected per $t_1$ increment. Shifted sine bells were used in both dimensions before Fourier transformation. The data were zero-filled to a 4096 × 4096 matrix. A polynomial baseline correction was performed. A delay of 5 s before each transient was used to allow complete longitudinal relaxation of the adenine H2 protons. The volume integration of each resolved cross-peak was measured on both sides of the diagonal. The distances between protons were then estimated using the distance extrapolation method (*15*). The intranucleotide distance between H5 and H6 protons of cytosine (2.45 Å) was used as a reference for distance calibration. The distances involving methyl groups were not taken into account because of uncertainties linked to the motions of these groups.

To measure vicinal $^3J_{H3'-P}$ coupling contants, the proton-detected selective heteronuclear experiment with a selective pulse on the H3′ protons described by Sklenár and Bax (*16*) was used as described elsewhere (*13*). The soft pulse was obtained with an i-SNOB-3 shape (*17*) with a flip angle of 180° to invert the H3′ spin population. The selection of the H3′ region is rather easy since, in DNA, these protons resonate in an isolated region. To measure $J_{H3'-P}$ coupling constants that were not overestimated, we first look for optimal conditions (*13*) for carrying out this experiment, notably, to reduce the line width of signals. At 53.1 °C in agreement with the helix stability and 9.4 T, the data were collected with 1K data points and 256 $t_1$ increments; 160 transients were collected per increment. The data were zero filled to a 2048 × 1024 matrix. The observed values of $^3J_{^{31}P-^1H3'}$ coupling constants were linked to the H3′−C3′−O−P torsional angle $\theta$ using the following proton phosphorus Karplus relationship: $J = 15.3 \cos^2 \theta - 6.1 \cos \theta + 1.6$ (*18*). The C4′−C3′−O−P torsional angle $\epsilon$ is then calculated by adding 120° to $\theta$. The digital resolution of this experiment was 0.5 Hz per point, leading to an accuracy for the measured coupling constant of ±0.5 Hz. For signals with large line widths, only an upper limit of $J_{H3'-P}$ can be obtained (for more detail, see ref *13*).

*Simulation Methodology*. The modeling and refinement procedure was the same as that described for the 16N

modeling (*10*). Determination of three-dimensional structures was carried out through molecular modeling using the JUMNA algorithm (JUnction Minimisation of Nucleic Acids) (*19*, *20*). Sugar puckers (phase and/or amplitude), torsion angles, and distances can be constrained in JUMNA to a fixed value or to specified lower and upper bounds (*10*, *21*−*23*). Constraint violations are prevented by a quadratic penalty energy term with a force constant of 6 or 12 kcal $mol^{-1}$ $Å^{-2}$ for distance constraints and 1000 kcal $mol^{-1}$ $deg^{-2}$ for dihedral constraints. Two force fields were used, namely, FLEX (*10*, *19*, *21*−*24*) and AMBER94 (*25*, *26*), that have been added to JUMNA version 10.0 (*27*). Analyses of oligomer conformations are carried out with the CURVES algorithm which calculates the optimal helical axis and a complete set of helical parameters (*20*). A systematic search of stable BI−DNA conformations as initial structures was carried out as previously described (*10*). In addition, NMR evidence of BII backbone features for 16M led us to generate BII conformations at steps (b) to (e) (see Figure 1). Seven initial structures were used: three for BI and four for BII. All the structures belong to the B-DNA family with sugars in a broad C2′-endo range, but present a wide diversity of helical parameters. rms values between these structures range from 1 to 2.7 Å. Last, we performed a refinement procedure starting from an A-DNA structure to test the ability of the methodology to converge under restraints to a B-structure directly pointed out by the experimental data. As previously described (*23*), in this particular case, very large constraints on backbone angles were added to the constraint set to prevent the occurrence of different crankshaft transitions during minimization when the sugar pucker changes from C3′-endo to C2′-endo. The average rms value between A and B starting structures reaches 3.5 Å. Back-calculations of NOESY spectra were performed using the iterative relaxation matrix approach IRMA (NMRchitect software package, 2.3 release, Biosym Inc.). In the refinement procedure, the constraints were applied to each starting structure in five successive steps. After each minimization, back-calculations of NOESY spectra and adjustments of distance bounds were performed. First, the sugar phases were constrained by imposing the NOE-derived intrasugar H1′−H4′ distances with bounds of ±10%. Second, the $\epsilon-\zeta$ dihedral variations calculated from the $^{31}P$ chemical shifts (*22*, *28*) were applied in constraints. Then, the most significant intranucleotide distances (namely, base H6/H8 with H1′, H2′, H2″, and H4′ sugar protons and with H5 of cytosine; H1′ with H2′ and H2″; and H2 of adenine with H1′) were added to the constraint list with bounds adjusted according to the estimated distance values as described by Kim et al. (*29*). Next, the following internucleotide distances were applied with bounds of ±0.3 Å: H6/H8 with H1′ and H2′, H5 of cytosine with H1′, and H2 of adenine with H1′, together with the H6/H8−H6/H8 internucleotide distances with bounds depending on the magnitude of the estimated distances (*29*). Finally, the H6/H8−H2″ internucleotide distances with bounds of ±0.3 Å were applied at a final step since they are known to be overestimated (*21*, *22*), and in addition in our case, some of these distances are unusually large. Thus, 134 intranucleotide distances and 83 internucleotide distances were applied during the refinement procedure for 16M, whereas 124 intranucleotide and 65 internucleotide distances were applied as constraints in the 16N modeling procedure. No constraint was applied for the nucleotides at the end of the oligomer. The number of internucleotide distances is all the more important as they define the fine structure of an oligonucleotide. Over the five most meaningful internucleotide distances that can be measured by NMR (H6/H8−H6/H8, H6/H8−H1′, H6/H8−H2′, H6/H8−H2″, and H6/H8−H3′), a satisfying average number of 3.2 internucleotide distances per group of two successive bases was applied in constraints during the modeling of 16M (2.5 for 16N). However, for steps which present irregularities in their backbone conformations, these five internucleotide distances were measured for both duplexes, and a comparison of NMR data and structures of the studied duplexes at these steps is therefore feasible. Only the H6/H8−H2″ cross-peak of steps (b) and (c) was sligthly superimposed in 16M, but sufficiently well-resolved to obtain reliable distances.

This iterative process is achieved when no more improvement in *R* factors is observed.

In the special case of steps (a) to (e) that are potently in BI−BII equilibrium, the resulting $^{31}P$ chemical shifts and NOE-derived distances are averaged between these two conformations. The $\epsilon-\zeta$ dihedral variations between BI and BII conformations are very large ($\epsilon-\zeta \approx -90°$ in the BI conformation and $\epsilon-\zeta \approx 90°$ in BII); therefore, the $\epsilon-\zeta$ angle was not constrained for these steps during the refinement of 16M structures. However, interproton distances measured for these steps were used as constraints in the refinement strategy to calculate *R* factors and energy cost to know whether the BI conformation is in better agreement with NMR data or BII.

## RESULTS AND DISCUSSION

### *Analysis of NMR Data*

*(a) Sugar Ring Conformation*. The short mixing time NOESY spectrum (15 ms) indicates C2′-endo conformations for the 16M sugar rings without any north−south equilibrium except for the sugars of the terminal nucleotides. These sugars exhibit dipolar interactions between aromatic protons and both H2′ and H3′ sugar protons as a result of conformational averaging. H1′−H4′ distances, which account well for sugar puckers, were introduced into the refinement strategy so the pseudorotational phase angles for each sugar conformation could be monitored and refined.

*(b) Proton and Phosphorus Resonances*. The small phosphorus signal dispersion, less than 1 ppm (Figure 2), indicates a right-handed helix for both duplexes. In addition, the strong correlations observed with a short mixing time (15 ms) in the NOESY experiment between base H6/H8 protons and H2′ or H2″ sugar protons of the same nucleotide indicate C2′-endo conformations for the sugars, and consequently B-type duplexes. The assignment of proton resonances was conducted using the classical methods for nucleic acids (*30*−*33*). Two different regions of the NOESY WATERGATE are shown in Figure 3. Strong interactions between imino protons of adjacent base pairs are observed (Figure 3a). Thymine N3H resonances (13.3−14.2 ppm) are well-separated from the guanine N1H resonances (12.4−13.1 ppm). Dipolar interactions between the thymine imino proton and the adenine H2 base proton of the same base pair enable preliminary assignments (Figure 3b). In addition, the thymine

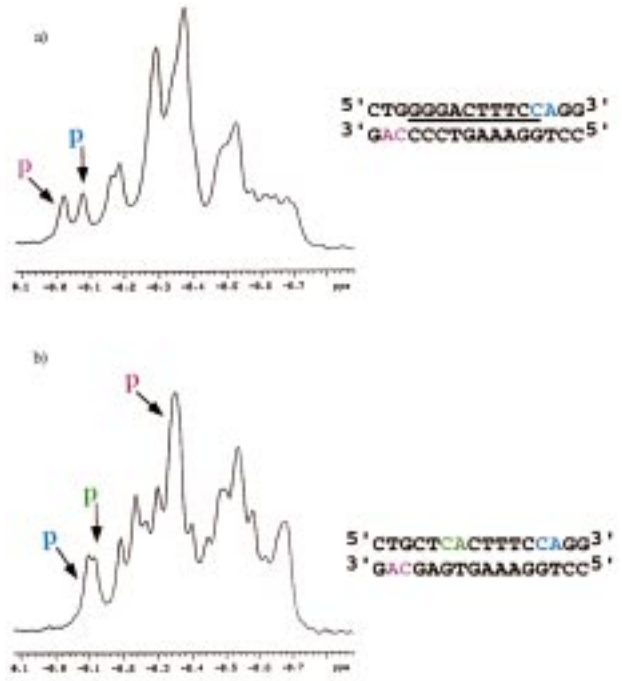


FIGURE 2: One-dimensional $^{31}$P spectra at 35 °C of (a) 16N and (b) 16M. The phosphates that exhibit peculiar behaviors in terms of chemical shifts and temperature are denoted in the same color as their corresponding steps. The underlined base pairs denote the 10 bp of the HIV-1 $\kappa$B site.

imino protons show dipolar interactions with H1′ sugar protons (Figure 3b), whereas the guanine imino protons exhibit dipolar interactions with the H5 protons of base-paired cytosines (Figure 3b). The cytosine amino protons were assigned through correlations with the guanine imino proton of the same base pair and also with the imino proton of the adjacent thymine. The amino protons of guanine and adenine were not observed due to an additional relaxation process involving these protons.

The $^{31}$P spectra of 16N (Figure 2a) and 16M (Figure 2b) exhibit a different distribution of phosphorus signals. Moreover, some of the $^{31}$P signals are strongly downfield-shifted. Since $^{31}$P chemical shifts are strongly related to backbone structural features (*10*, *13*, *22*, *34*, *35*), all the phosphorus resonances for the two duplexes were assigned (*10*, *13*). Knowledge of the backbone conformation is all the more relevant as numerous phosphates are contacted by the p50-p65 heterodimer in the crystal structure (*7*). The table in the Supporting Information gives the proton and phosphorus chemical shifts of 16M. Only the resonances of nuclei around the mutation are significantly different between 16N and 16M. Thus, differences of structure, if any, should be searched for around the mutation. For both duplexes, signals that exhibit the most downfield-shifted resonances (Figure 2) were assigned to phosphorus resonances involved in CpA steps, steps (b) and (c) for 16N and (c) and (e) for 16M. On the contrary, the $^{31}$P chemical shift of CpA (b) in 16M exhibits a strong upfield shift. These downfield-shifted $^{31}$P resonances should indicate an irregular conformation of the phosphodiester backbone at these steps.

*(c) Minor Groove Size*. The interstrand distances between adenine H2 base protons and H1′ sugar protons are sensitive to the DNA minor groove width. A significant interstrand NOE interaction between the A7 H2 base proton and the C27 H1′ sugar proton in 16N was observed no matter which mixing time was used, and the extrapolated distance was approximately 3.7 Å. On the contrary, for 16M, a very weak NOE interaction between the A7 H2 base proton and the G27 H1′ sugar proton appears only for mixing times of >150 ms, and the resulting distance was approximately 5.9 Å, that is, to the limit of interactions that can be measured and quantified. The AH2−H1′ interstrand interactions are however quite similar in the case of the 3′-end adenines of both duplexes. These differences between 16N and 16M in interstrand NOE interactions were previously observed for the larger 24 bp fragments encompassing the $\kappa$B site and one of the Sp1 sites (*36*). They suggest a wider minor groove for 16M that could induce changes in the major groove geometry where NF-$\kappa$B binds.

*(d) Analysis of the Phosphodiester Backbone*. 5′Pyrimidine-purine3′ sequences are known to frequently be associated with the BI−BII equilibrium (*10*, *12*, *28*, *34*, *37*−*39*). Crystallographic structures often exhibit these BII conformations (*40*). More recently, significant BII-populated phosphates have been highlighted in solution by various NMR data (*10*,

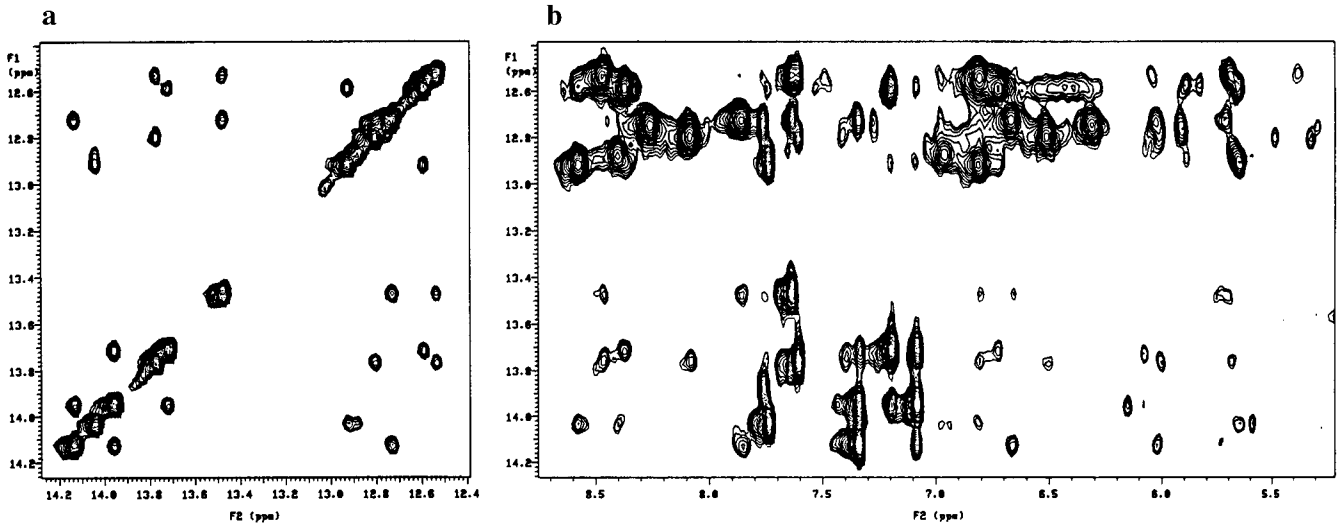


FIGURE 3: Results from a NOESY WATERGATE experiment carried out at 25 °C with a mixing time of 150 ms. On the left are shown the interactions between imino protons and on the right the interactions between imino protons ($F_1$ dimension) and adenine H2 base protons, cytosine amino and H5 protons, and H1′ sugar protons ($F_2$ dimension).

*28*). These studies clearly fixed the NMR data that enable us to highlight the presence of a BI−BII equilibrium in solution. First, the significant BII-populated phosphates exhibit downfield $^{31}$P chemical shifts, which shift upfield upon temperature increases. In addition, Gorenstein (*39*) analyzed the H3′−P coupling constant in terms of fractional populations of BI and BII conformations and stated that a large H3′−P coupling constant indicates a large BII population. A study of highly resolved crystallographic B-DNA structures (*40*) enabled us to obtain the mean value of the $\epsilon$ angle. For BI phosphates, the mean $\epsilon$ angle reaches −176°, whereas it is −114° for BII ones. Therefore, the corresponding $J_{H3'-P}$ values range from 1 Hz in the BI conformation to 11 Hz in BII. In solution, the H3′−P coupling constant can thus be interpreted in terms of fractional populations of BI and BII conformations. Second, NOE-derived internucleotide distances are larger when a BII conformation occurs, particularly for the base H6/H8 and sugar H2″ internucleotide distances. Finally, the H1′ chemical shifts exhibit the largest downfield shift variations when the temperature is increased for steps involved in the BI−BII equilibrium (*10*), probably as a result of sugar movement of these steps (*41*).

In Table 1, we summarize the NMR data for 16M and 16N that can discriminate between BI and BII conformations of the phosphodiester backbone.

NMR data for steps (c) and (d) are similar for both duplexes and confirm that the mutation has little effect on the 3′-end of 16M. Consequently, steps (c) and (d), as mainly indicated by downfield $^{31}$P resonances and large $J_{H3'-P}$ coupling constants, together with large H6/H8−H2″ internucleotide distances, also undergo BI−BII transitions in 16M as in 16N.

For steps (a) and (b) of 16M, near the mutation, NMR data exhibit differences in the backbone conformation with respect to 16N. In 16M, for these two steps, $^{31}$P resonances are strongly upfield shifted as a result of a displacement of the BI−BII equilibrium toward the BI conformation. In addition, for step (a) in 16M, the downfield $^{31}$P chemical shift variation upon temperature increases; the small H3′−P coupling constant and the small internucleotide H6/H8−H2″ distance imply that the BII (a) conformer is not significantly populated or may even be nonexistent. For step (b), the situation is more complicated since its $^{31}$P chemical shift and variation with temperature are in favor of a BI conformation, whereas the mean internucleotide H6/H8−H2″ distance and the large H3′−P coupling constant are rather in favor of a still significant BII population. Moreover, the C30 H1′ chemical shift, as well as its variation with temperature, would indicate a majority in the BI population for step (b) in 16M. Concentration effects cannot account for this since no difference is observed for site (c) or (d). Therefore, for step (b), the BII conformer is obviously less populated in 16M than in 16N, but it is not clear if a significant population of the BII conformer is still present.

Finally, the mutation has introduced a 5′pyrimidine-purine3′ sequence at steps (e) and (f). Only the NMR data for step (e) in 16M exhibit the characteristics of a BI−BII equilibrium like steps (c) and (d).

Therefore, NMR data for 16M are in agreement with significant BII populations for steps (c), (d), and (e). A rather small population of the BII conformer may be present in solution for step (b). As already demonstrated for 16N (*10*), NMR results for steps (c) and (d) are in favor of two BII conformations facing each other in the duplex. In addition, modeling has already suggested the fact that two BII conformations facing each other are more stable than a single BII site (*12*, *41*). Such calculations performed on the 16M duplex confirm this result and show that structures with simultaneous BII conformations at steps (c) and (d) are as stable as the BI conformations. Thus, for the molecular modeling of 16M, three BII conformations generated at steps (c), (d), and (e) were considered leading to structures **e**, **cd**, and **cde** (see Materials and Methods for more details). Moreover, to investigate the presence of a potential BII population for step (b), a BII conformation at step (b) was also generated (named structure **b**).

Table 1: NMR Data for 16N and 16M Characterizing the Conformation of the Phosphodiester Backbone[a]

| steps | NMR data | 16M | 16N |
|---|---|---|---|
| | sequence | Y**TpG**YY | Y**TpG**RR |
| | $\delta(^{31}P)$ (ppm) | −0.41 | −0.28 |
| | $\Delta[\delta(^{31}P(T))]$ (ppm) | 0.08 | −0.05 |
| (a) | $J_{H3'-P}$ (Hz) | 4.8 ± 0.5 | nm |
| 2 and 3 | $d$(H6/H8−H2″) (Å) | 2.8 | 3.5 |
| | $\delta(^1H)$ (ppm) | 5.84 | 5.72 |
| | $\Delta[\delta(^1H)](T)$ (ppm) | 0.05 | 0.09 |
| | sequence | RR**CpA**R | YY**CpA**R |
| | $\delta(^{31}P)$ (ppm) | −0.37 | −0.02 |
| | $\Delta[\delta(^{31}P(T))]$ (ppm) | 0.03 | −0.14 |
| (b) | $J_{H3'-P}$ (Hz) | 5.6 ± 0.5 | nm |
| 30 and 31 | $d$(H6/H8−H2″) (Å) | 3.1 | 4.0 |
| | $\delta(^1H)$ (ppm) | 5.54 | 5.33 |
| | $\Delta[\delta(^1H)](T)$ (ppm) | 0.09 | 0.2 |
| | sequence | YY**CpA**RR | YY**CpA**RR |
| | $\delta(^{31}P)$ (ppm) | −0.12 | −0.08 |
| | $\Delta[\delta(^{31}P(T))]$ (ppm) | −0.04 | −0.1 |
| (c) | $J_{H3'-P}$ (Hz) | 5.5 ± 0.5 | nm |
| 13 and 14 | $d$(H6/H8−H2″) (Å) | 3.3 | 3.6 |
| | $\delta(^1H)$ (ppm) | 5.28 | 5.27 |
| | $\Delta[\delta(^1H)](T)$ (ppm) | 0.09 | 0.11 |
| | sequence | YY**TpG**RR | YY**TpG**RR |
| | $\delta(^{31}P)$ (ppm) | −0.34 | −0.30 |
| | $\Delta[\delta(^{31}P(T))]$ (ppm) | 0 | −0.06 |
| (d) | $J_{H3'-P}$ (Hz) | $<5.7 \pm 0.5$ | nm |
| 19 and 20 | $d$(H6/H8−H2″) (Å) | 3.1 | 3.4 |
| | $\delta(^1H)$ (ppm) | 5.64 | 5.63 |
| | $\Delta[\delta(^1H)](T)$ (ppm) | 0.06 | 0.06 |
| | sequence | YY**CpA**YY | RR**GpA**YY |
| | $\delta(^{31}P)$ (ppm) | −0.14 | −0.37 |
| | $\Delta[\delta(^{31}P(T))]$ (ppm) | −0.02 | −0.01 |
| (e) | $J_{H3'-P}$ (Hz) | 5.3 ± 0.5 | nm |
| 6 and 7 | $d$(H6/H8−H2″) (Å) | 3.2 | nm |
| | $\delta(^1H)$ (ppm) | 5.44 | 5.53 |
| | $\Delta[\delta(^1H)](T)$ (ppm) | 0.07 | 0.05 |
| | sequence | RR**TpG**RR | RR**TpC**YY |
| | $\delta(^{31}P)$ (ppm) | −0.55 | −0.19 |
| | $\Delta[\delta(^{31}P(T))]$ (ppm) | 0.03 | 0 |
| (f) | $J_{H3'-P}$ (Hz) | 4.5 ± 0.5 | nm |
| 26 and 27 | $d$(H6/H8−H2″) (Å) | 2.9 | nm |
| | $\delta(^1H)$ (ppm) | 5.76 | 6.01 |
| | $\Delta[\delta(^1H)](T)$ (ppm) | 0.01 | 0.02 |

[a] Sequence indicates the sequence context for each considered step in bold (Y for pyrimidine and R for purine). $\delta(^{31}P)$ is the chemical shift of phosphorus at 35 °C. $\Delta[\delta(^{31}P(T))]$ is the variation of the phosphorus chemical shift when the temperature is increased from 35 to 55 °C [$\delta$(55 °C) − $\delta$(35 °C)]. $J_{H3'-P}$ is the H3′−P coupling constant measured for 16M at 55 °C. The sign < indicates that only an upper limit of $J$ can be determined. $d$(H6/H8−H2″) is the internucleotide distance between the H6/H8 proton of the purine and the H2″ sugar proton of the pyrimidine derived from NOE data. $\delta(^1H)$ is the chemical shift of the H1′ sugar proton of the pyrimidine. $\Delta[\delta(^1H)](T)$ denotes the variation of the H1′ sugar proton of the pyrimidine chemical shift when the temperature is increased from 35 to 55 °C [$\delta$(55 °C) − $\delta$(35 °C)].

Table 2: Averages of *R* Factors for the BI and BII Families[a]

| | $R$ | $R_{1/6}$ | $R_{intra}$ | $R_{1/6-intra}$ | $R_{inter}$ | $R_{1/6-inter}$ | $R$(c) | $R_{1/6}$(c) | $R$(d) | $R_{1/6}$(d) | $R$(e) | $R_{1/6}$(e) | $R$(b) | $R_{1/6}$(b) | $R_{28-29}$ | $R_{1/6-28-29}$ | $R_{24-25}$ | $R_{1/6-24-25}$ |
|---|---|---|---|---|---|---|---|---|---|---|---|---|---|---|---|---|---|---|
| BI | 0.36 | 0.07 | 0.29 | 0.06 | 0.60 | 0.09 | 0.29 | 0.07 | 0.31 | 0.07 | 0.41 | 0.09 | 0.35 | 0.07 | 0.24 | 0.05 | 0.38 | 0.06 |
| **cd** | 0.34 | 0.06 | 0.28 | 0.06 | 0.55 | 0.08 | 0.25 | 0.05 | 0.22 | 0.04 | 0.39 | 0.08 | 0.33 | 0.07 | 0.23 | 0.05 | 0.38 | 0.07 |
| **cde** | 0.35 | 0.06 | 0.29 | 0.06 | 0.56 | 0.08 | 0.24 | 0.05 | 0.23 | 0.04 | 0.42 | 0.08 | 0.31 | 0.06 | 0.24 | 0.05 | 0.38 | 0.07 |
| **e** | 0.36 | 0.07 | 0.29 | 0.05 | 0.61 | 0.09 | 0.28 | 0.07 | 0.28 | 0.06 | 0.42 | 0.08 | 0.31 | 0.06 | 0.23 | 0.05 | 0.38 | 0.07 |
| **b** | 0.38 | 0.07 | 0.30 | 0.06 | 0.67 | 0.10 | 0.30 | 0.07 | 0.37 | 0.07 | 0.39 | 0.08 | 0.64 | 0.12 | 0.28 | 0.06 | 0.40 | 0.07 |

[a] $R$ and $R_{1/6}$ values were calculated for the whole oligomer; $R_{intra}$ (or $R_{inter}$) and $R_{1/6-intra}$ (or $R_{1/6-inter}$) were calculated over all the intranucleotide (or internucleotide) distances used in the refinement. Local $R$ factors for different steps were also calculated, and the letter indicates the step involved. $R = \Sigma|V_{exp} - V_{sim}|/\Sigma V_{exp}$, and $R_{1/6} = \Sigma|V_{exp}^{1/6} - V_{sim}^{1/6}|/\Sigma V_{exp}^{1/6}$, where the summation runs over all peaks of interest for mixing times of 150, 200, and 250 ms, $V_{exp}$ is the NOE intensity, and $V_{sim}$ is the simulated NOE intensity.

*(e) Importance of the Neighboring Sequence for BI−BII Transitions at 5′Pyrimidine-Purine3′ Steps*. The flexibility of some YpR steps has originally been suggested by Ulyanov et al. (*42*). Within these two duplexes, 10 CpA and TpG steps occur in different sequence contexts. A previous molecular modeling study demonstrated that $(Y)_n$**YpR**$(R)_n$ sequences make the BI−BII transition easier for the central **YpR** steps (*12*). NMR data for these steps enable us to reinforce our findings concerning the effect of neighboring sequences on pyrimidine-purine backbone flexibility. Here, a significant BII population has been clearly demonstrated for seven steps (CpA or TpG; see Table 1). Six sites are present in a **(Y)Y**YpR**R(R)** sequence context (two BII facing each other) and one in a **YY**YpR**YY** sequence context (single BII on one strand), which strengthen previous results (*28*). Therefore, BII conformers seem to be present in a majority at 5′pyrimidine-purine3′ steps with YY sequence at their 5′-side and preferably with RR sequence at their 3′-side.

## *Molecular Modeling and Structural Analysis of the Mutated Duplex*

*(a) Modeling Strategy*. As explained in the previous section, two families of initial structures were generated: the BI family with all the phosphodiester backbone in BI conformations and the BII family with the phosphate groups at steps (b) to (e) in BII conformations leading to structures **b**, **e**, **cd**, and **cde**. Constraints ($\epsilon-\zeta$ dihedral angle differences and interproton distances) were applied during the refinement procedure as previously described (*10*) using two different force fields. Independent of the force field used, the refinement procedure led to a set of very similar structures in terms of energy, helical parameters, and rms. This involved an average rms of 0.8 Å between structures within the BI family. A similar rms was also obtained among the **cd** structures. Note that between refined and starting structures, the rms typically ranges from 1.3 to 1.6 Å. Moreover, the data from a refinement procedure conducted with an A-DNA as a starting point rapidly converge under NMR data to the B-structure already obtained.

The refinement procedure leads to an energy cost of 17 kcal mol$^{-1}$ for **cd** structures, 19 kcal mol$^{-1}$ for the BI family, 21 kcal mol$^{-1}$ for **cde** and **e** structures, and 25 kcal mol$^{-1}$ for **b** ones. Thus, compared to free minimizations, the energetics of the refined structures seems to indicate that BII conformations at steps (c) and (d) are more favorable than BI conformations.

Table 2 gives the averages of $R$ and $R_{1/6}$ factors over the set of refined structures for the BI family and for the four BII family structures. $R$ factors for the whole oligonucleotide are equivalent for all structures and decreased by roughly 36% for $R$ and 29% for $R_{1/6}$ during the refinement. Only a small decrease in the $R$ factor is seen for intranucleotide distances ($R_{intra}$) during the refinement procedure, which is not surprising as intranucleotide distances mainly define the helix type and do not vary significantly within the B-DNA family. On the contrary, $R$ factors over internucleotide distances ($R_{inter}$) which define the fine structure of an oligonucleotide show large variations during the refinement procedure. For the BI family and the **cd** structures, $R_{inter}$ exhibits an improvement of 56% and $R_{1/6}$ of 41%. $R_{inter}$ factors are slightly better for the **cd** and **cde** structures. Local $R$ factors were calculated for steps (b) to (e), together with local $R$ factors for steps 24 and 25 and 28 and 29 used as references. The local $R$ factors calculated for steps (c) and (d) for **cd** or **cde** structures confirm that BII conformations at steps (c) and (d) agree better with NMR data. These results are consistent with the fact that the **cd** conformations are the most stable and energy loss during refinement is the smallest. For step (e), both conformations lead to the same $R$ factors, and therefore, BI and BII conformations are both compatible with NMR data. For step (b), the local $R$ factors are very poor and suggest that the BII conformation does not agree with the NMR data.

To conclude, after refinement, both energetic and structural considerations indicate that BII conformers are present in a majority at steps (c) and (d), with the same probability as a BI conformer at step (e), and with no significant BII population at step (b).

*(b) Backbone Conformation and Helical Parameter Analysis*. NMR structures derived by NOE calculation are underdetermined (*43*−*45*). However, twist, roll, shift, and slide helical parameters can be determined accurately with NMR data (*45*). The great number of internucleotide distances and $\epsilon$ and $\zeta$ difference angles obtained for this duplex enables us to precisely define these parameters. As suggested by the rms values, the refined structures from a given family exhibit very similar helical parameters. From a set of different structures (maximal rms of 4 Å, including the A-DNA starting point), the refinement procedure conducted with two different force fields leads to families of structures with appreciably low rms values. Therefore, all helical parameters seem to be well-defined, and only small scatters around the average of helical parameters are observed (data not shown). The largest variations of parameters are observed for the BI refined structures for the $X_{disp}$ (maximal variation of 0.7 Å) and for the inclination (maximal variation of 8°). Moreover, the helical parameters show the same variation profile along the sequence for all the refined structures within each family.

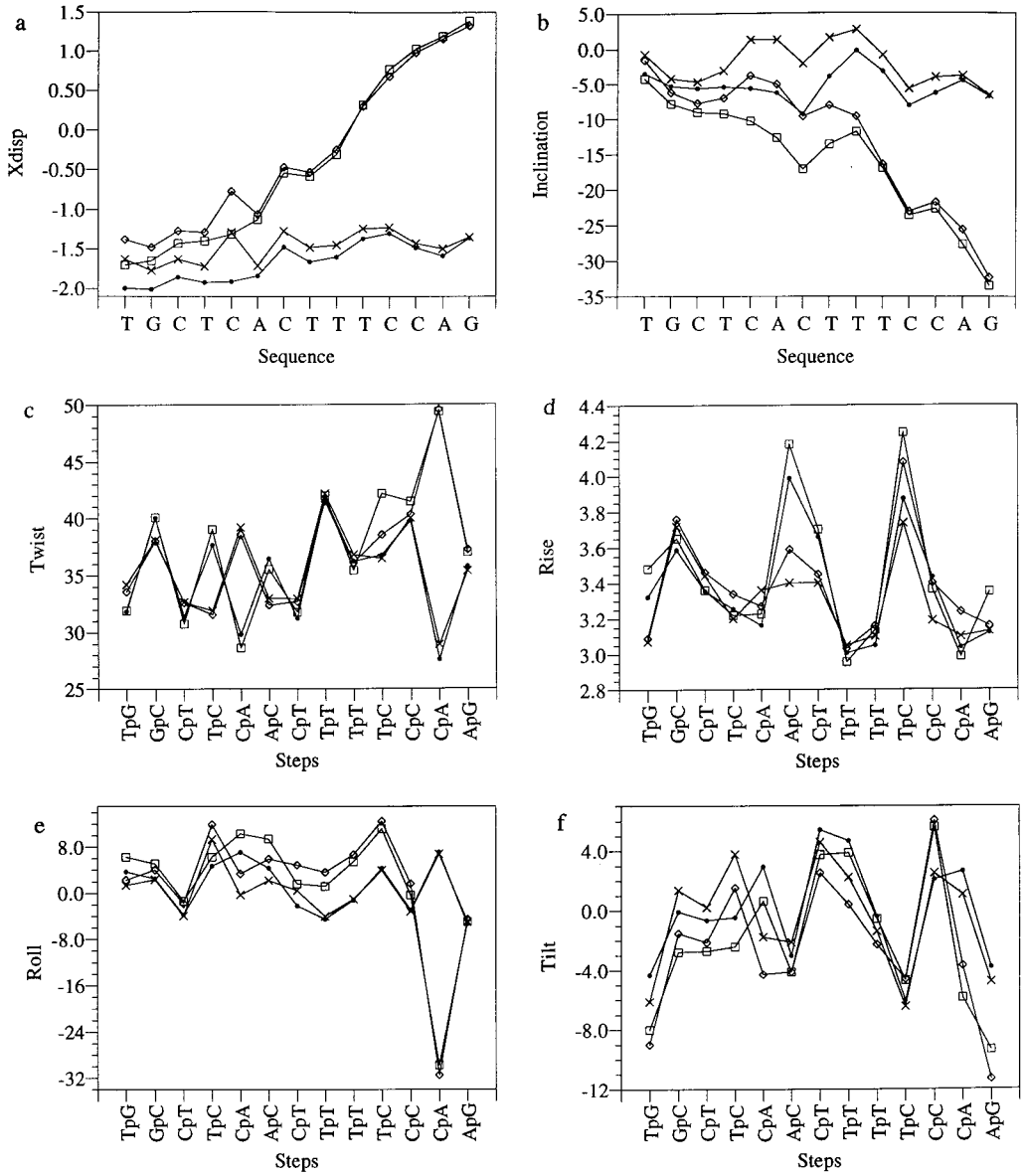


FIGURE 4: Analysis of average helical parameters (●) for BI structures, (□) for **cd** structures, (◇) for **cde** structures, and (×) for **e** structures: (a) $X_{disp}$, (b) inclination, (c) twist, (d) rise, (e) roll angle, and (f) tilt.

This is in constrast to the random variation of helical parameters along the sequence in the starting structures. Consequently, for the purpose of clarity, only average values of helical parameters calculated over the refined structure sets are presented in Figure 4 for the BI and BII families (structures **e**, **cd**, and **cde**). Average values of $\epsilon-\zeta$ dihedral differences for each strand are given in Figure 5.

*BI Family.* Average helical parameters for the BI family are canonical for a B-DNA with an $X_{disp}$ of −1.7 Å, a twist of 35° for a rise of 3.4 Å, and an inclination of −5°. The BI $\epsilon-\zeta$ values are spread over a large range from −80° to −30° (Figure 5a,b). The three most stable structures for the BI family are presented in Figure 6. A good superposition is observed. All structures in the BI family exhibit a straight helix axis.

*BII Family.* As previously observed (*41*), the generation of a BII conformation on only one strand of the oligomer, like at step (e), does not lead to large helical distortions. The effect is very local for twist and $X_{disp}$ values, and globally, the overall helical parameters for structure **e** (or **cde**) exhibit the same variations as those for BI structures (or **cd**). In the case of structure **e** or **cde**, the twist values for CpA at step (e) exhibit a higher magnitude than for the other structures followed by a variation of twist values on both sides of this step. These results fit with rms values obtained for the half-site of 16M. Indeed, rms values were calculated for nucleotides from position 2 to 7 and from position 7 to 15. For the first half of 16M, BI structures superimpose well with structures **cd** (average rms of 0.2 Å) and quite well with structures **cde** and **e** (average rms of 0.6 Å). On the contrary, for the second half of 16M (positions 7−15), BI structures exhibit rms values of around 2.5 Å when superimposed with structures **cd** or **cde**. Such a large rms is not surprising since the phosphodiester backbone conformation at steps (c) and (d) and the associated parameters are completely different in structures **cd** and **cde** (BII conformation) compared to those in the BI family (BI conformation).

As previously described, the movements of two phosphates facing each other changing from BI to BII generate $X_{disp}$, roll, twist, and inclination variations (*10*, *12*, *41*, *45*). In the

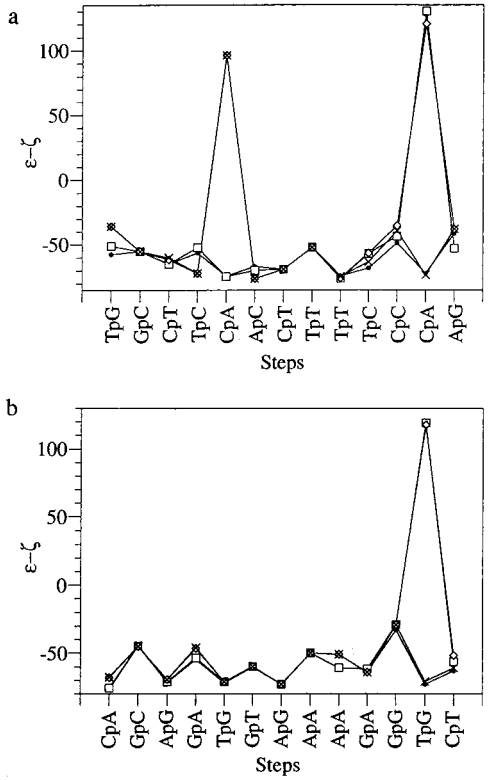


FIGURE 5: $\epsilon-\zeta$ dihedral variations (●) for BI structures, (□) for **cd** structures, (◇) for **cde** structures, and (×) for **e** structures: (a) first strand 5′ → 3′ and (b) complementary strand 3′ → 5′.

case of CpA (c)·TpG (d), a high twist value (50°) is characteristic of two facing BIIs in the duplex for structures **cd** and **cde**. However, this large twist has little effect on the adjacent twist values (Figure 4c). Similarly, the roll angle becomes strongly negative and creates a local kink toward the minor groove (Figure 4e). A major effect of simultaneous BII transitions is that $X_{disp}$ and inclination change not only at the BII sites but also for the 5 bp surrounding the BII sites (Figure 4a,b). The movements of the phosphates at steps (c) and (d) push away these base pairs into the major groove, but also the base pairs of the second part of the duplex to reduce the extent of destacking. Thus, we observe strongly positive $X_{disp}$ values (Figure 4a) linked to negative inclination (Figure 4b) which gradually decreases toward the 5′-base pairs. Only the base pairs of the second part of the duplex are translated toward the major groove.

The helix axis is roughly straight when only the base pairs from positions 2 to 13 are analyzed with CURVES. However, when the whole oligomer (from position 2 to 15) is analyzed, a global curvature of 30° toward the major groove appears due to kinks at steps (c) and (d). The three most stable **cd** structures are shown in Figure 6. The helix axis is rather straight on the first part of the oligomer and begins kinking toward the major groove at the 3′-end of the duplex.

The BII sites clearly appear with $\epsilon-\zeta$ values ranging from 100° to 130° (Figure 5) associated with a decrease of $\beta$ from approximately 170° to 130°. $\epsilon-\zeta$ values for the other steps are quite similar to those observed for the BI families (Figure 5a,b).

### *Structural Comparison of the Native and Mutated κB Site*

*(a) Helical Parameters*. To analyze the mutation effects on the three-dimensional structure, the helical parameters that present the largest variations are presented in Figure 7 for the BI and BII families of 16N and 16M. The 16M BII family encompasses refined **cd** structures since the **cde** structures have been shown to behave like **cd** structures. The 16M **e** structures present the same variation of helical parameters as the 16M BI structures. The 16N BII family regroups refined **abcd** structures (using the same nomenclature that was used for 16M) together with refined **cd** structures since this conformation can potentially exist in solution, and the comparison with **cd** structures of 16M seems relevant. For the purpose of clarity, only the mean values of helical parameters for each family are indicated. In the guanine tract of 16N, $X_{disp}$ values are always less negative than for the other base pairs, whereas the inclination is strongly negative. While for the BI family the average twist in the G-tract is around 37°, in 16M, the mutation induces an alternation of low and high twist values. These large structural variations between 16N and 16M agree with the large differences observed in NMR spectra of both duplexes around the mutation.

When the helical parameters at the 3′-end of the duplexes are compared, the range of values is quite similar for the BI and BII families. rms values calculated for nucleotides 7−15 have an average value of 1.2 Å for 16M BI structures superimposed with 16N BI structures and of 1 Å for 16M **cd** structures superimposed with 16N BII structures. Small variations of twist and roll values are observed for the CpC step, but only one internucleotide distance was derived from NMR data; this step is obviously underdetermined.

For both duplexes, the generation of **cd** structures leads to the same distortions. Two BII conformations facing each other in the duplex generate helical distortions over 5 bp characterized by a strongly positive $X_{disp}$ and a negative inclination. For 16N, in the case of four simultaneous BII conformations, 5 bp at the 5′-side and at the 3′-side are affected, and consequently, all 10 bp of the κB site are pushed toward the major groove.

*(b) Groove Geometry*. Table 3a gives the average values of the minor groove width and major groove depth for BI or BII steps for studying the effect of two BII transitions facing each other in the duplex. "BI steps" implies that the average is calculated for all steps in the BI conformation for both duplexes. To calculate the average values of groove dimensions with BII steps, we first examined the extent of nucleotides for which grooves are influenced by BII steps facing each other. For two simultaneous BII steps at the 5′-end of the oligomer (or 3′-end), averages are calculated for nucleotides 3, 4, and 5 (or 11, 12, and 13). The major effect of BII sites facing each other in the duplex clearly lies in making the minor groove narrower and the major groove much less deep in agreement with the unusual values of $X_{disp}$ and inclination.

NMR data showed a narrowing of the minor groove for 16N. GC-rich DNA oligonucleotides have already been reported with narrow minor grooves (*46*). To explain this feature, the authors suggested that buckles at $R_nY_m$ junctions become strongly positive, shortening the minor groove and consequently making the interstrand H2−H1′ distances measurable by NMR. In fact, the mean of the buckle angles within the G-tract of 16N reaches 12°, whereas it is around −5° in 16M. To investigate the influence of a G-tract on the major groove size, the average major groove width and

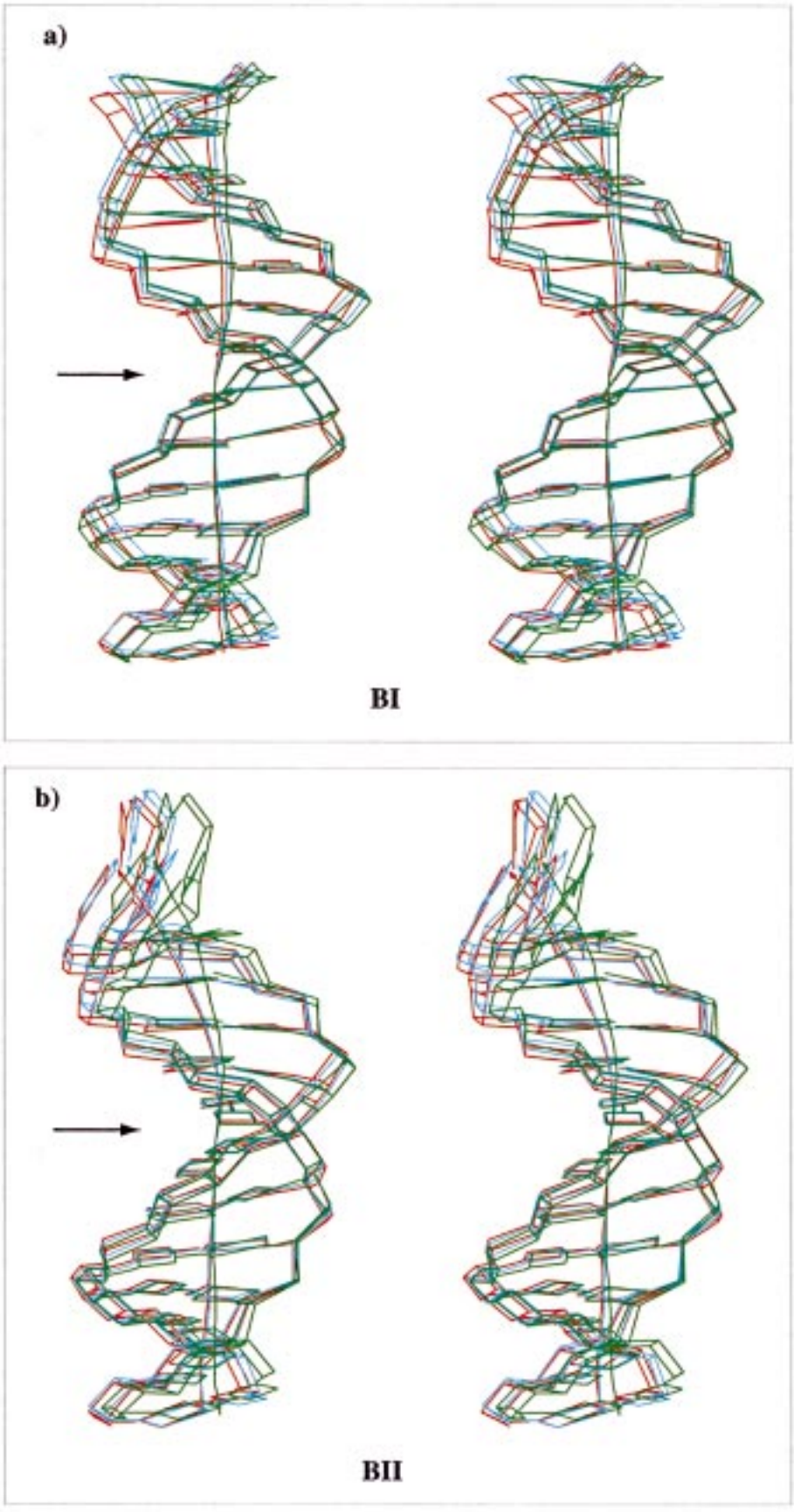


FIGURE 6: Stereoview of the three most stable structures for each family of 16M. For the BI structures (top) and the **cd** structures (bottom), the black arrow indicates the direction of the major groove. The graphic representation was created with CURVES.

depth, independent of the conformation of the phosphodiester backbone for 16N and 16M, are given in Table 3b. Major groove depths were also indicated according to the backbone conformation since Table 3a showed that BII steps made

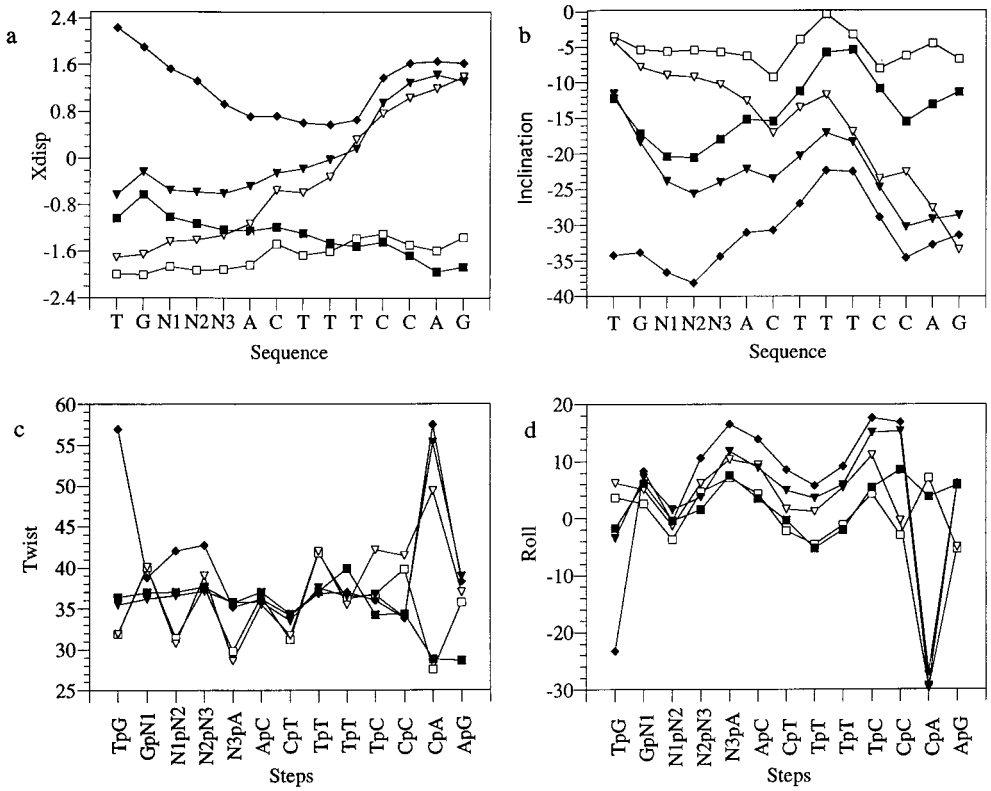


FIGURE 7: Comparison of average helical parameters between the native and the mutated duplexes: (■) BI structures and 16N, (▼) **cd** structures and 16N, (◆) **abcd** structures and 16N, (▽) **cd** structures and 16M, and (□) BI structures and 16M.

Table 3: Groove Sizes[a]

| (a) | minor groove width (Å) | major groove depth (Å) |
|---|---|---|
| BI steps | 4.8 | 5.1 |
| BII steps | 2.0 | 0.4 |

| (b) | | major groove width (Å) | major groove depth (Å) | |
|---|---|---|---|---|
| | BI | | 4.1 | |
| 16N | **abcd** | 15.5 | 1.9 | **3.2** |
| | **cd** | | 3.7 | |
| 16M | BI and **e** | 12.5 | 5.8 | **6.1** |
| | **cd** and **cde** | | 6.3 | |

[a] (a) Average of the minor groove width and the major groove depth as a function of the conformation of the phosphodiester backbone. "BI steps" means that the average is calculated for all BI steps in both duplexes. "BII steps" means that the average is calculated for nucleotides 3, 4, and 5 and 11, 12, and 13 within BII refined structures of both duplexes. (b) Average of the major groove width and depth over the refined structure sets of 16N and 16M. Averages of the major groove depths are denoted in bold. Major groove depths are also indicated as a function of the conformation of the phosphodiester backbone. The analysis runs over nucleotides from position 3 to 8.

the major groove shallower. The G-tract clearly widens the major groove and makes it less deep no matter which structure is considered. Thus, 16M has a deeper and narrower major groove that could hinder protein approach.

## CONCLUSION

NMR data for 16M highlighted the fact that a 3 bp mutation within the NF-$\kappa$B binding site implies a different distribution of the conformational equilibrium of the phosphodiester backbone around the mutation and large changes in helical parameters. The BI−BII equilibrium of the CpA·TpG dinucleotide at the 5′-end of 16N disappears for 16M, but the CpA·TpG dinucleotide at the 3′-end of 16M still presents a BI−BII equilibrium. In addition, step (e) exhibits a BI−BII equilibrium, but a BII conformation within only one strand leads to minor perturbations. Therefore, for the mutated sequence, two families of models are proposed: one with the entire phosphodiester backbone in BI conformations and the second with steps (c) and (d) in BII conformations. The two sets of refined structures are in good agreement with NMR data with respect to their *R* factors. However, local *R* factors calculated for steps (c) and (d) are better when BII conformations are considered, indicating that BII conformers at these steps are clearly dominant. The BI refined structures are canonical B-DNAs. Two simultaneous BII transitions in both strands induce local curvature of the helix axis and change in the major groove dimensions and influence the $X_{disp}$ and the inclination of the five neighboring base pairs to maintain good base pair stacking. For 16N, five base pairs are affected by each BI−BII equilibrium occurring upstream or downstream of the 10 bp $\kappa$B site and thus influence the structure of the whole site. Therefore, 16N can reach a conformation very favorable for the interaction with NF-$\kappa$B, which presents a helical axis curvature in the same direction as in the NF-$\kappa$B−DNA crystal complexes and a translation of all the $\kappa$B base pairs toward the major groove. 16M cannot mimic such a conformation, and moreover, groove dimensions in 16M could hinder the DNA−protein interactions.

The question of the mechanism of the specific recognition of DNA by proteins remains to be solved. Structural studies over the past 15 years have provided very useful information about the protein motifs that interact with DNA and of the DNA distortions in the protein−nucleic acid complexes.

However, although the deformability and flexibility of DNA seem to be highly important, structural studies of native and mutated duplexes generally reveal only small differences that cannot explain the different protein binding behaviors. The role played by DNA in protein−DNA interaction is not clearly established, but it is acknowledged that localized DNA conformational changes may help to maximize protein interactions and are thus likely to be stabilized in the complex.

Here, we have presented the NMR solution structure of a mutated κB site that helps in understanding the specific recognition of κB sites by NF-κB. The 3 bp mutation within the NF-κB binding site changes the BI−BII conformational equilibrium within the phosphodiester backbone near the mutations and implies important coupled changes in helical parameters. We have demonstrated that the deformability of the native duplex enables it to reach a conformation with an intrinsic global curvature of the helix axis toward the major groove and a translation of all the base pairs into the major groove. In contrast, the mutated duplex can only kink at its 3′-end, and only the base pairs at this side can move toward the major groove. Moreover, the major groove is narrower and the base pairs are more buried than in the native duplex. To our knowledge, for the NF-κB−DNA crystal complexes, the intrinsic properties of the native duplex are very favorable for the binding of NF-κB in contrast to that of the mutated duplex.

The results obtained for both duplexes also stress the importance of flanking sequences for the backbone flexibility of pyrimidine-purine steps within a $Y_nR_m$ sequence context. BI−BII equilibria of the phosphodiester backbone on each side of the κB site influence the structure of the whole site. Thus, sequence context effects, both upstream and downstream of a DNA binding site, can play an important role in providing an effective protein binding site.

## ACKNOWLEDGMENT

We thank Dr. Richard Lavery for helpful discussions.

## SUPPORTING INFORMATION AVAILABLE

Table giving proton and phosphorus chemical shifts of the mutated κB site, where temperatures are indicated in parentheses, light shadows denote the nuclei involved in the mutated nucleotide, and heavy shadows denote the nucleus significantly shifted in comparison with 16N (differences of >0.05 ppm). This material is available free of charge via the Internet at http://pubs.acs.org.

## REFERENCES

1. Nabel, G., and Baltimore, D. (1987) *Nature 326*, 711−713.
2. Clark, L., Matthews, J. R., and Hay, R. T. (1990) *J. Virol. 64*, 1335−1344.
3. Virelizier, J. L. (1990) *Curr. Opin. Immunol. 2*, 409−413.
4. Ghosh, G., Van Duyne, G., Ghosh, S., and Sigler, P. S. (1995) *Nature 373*, 303−310.
5. Müller, C. W., Rey, F. A., Sodeoka, M., Verdine, G. L., and Harrison, S. C. (1995) *Nature 373*, 311−317.
6. Cramer, P., Larson, C. J., Verdine, G. L., and Müller, C. W. (1997) *EMBO J. 16*, 7078−7090.
7. Chen, F. E., Huang, D.-B., Chen, Y.-Q., and Ghosh, G. (1998) *Nature 391*, 410−413.
8. Chen, Y.-Q., Ghosh, S., and Ghosh, G. (1998) *Nat. Struct. Biol. 5*, 67−73.
9. Schreck, R., Zorbas, H., Winnacker, E. L., and Baeuerle, P. A. (1990) *Nucleic Acids Res. 18*, 6497−6502.
10. Tisné, C., Hantz, E., Hartmann, B., and Delepierre, M. (1998) *J. Mol. Biol. 279*, 127−142.
11. Müller, C. W., Rey, F. A., and Harrison, S. C. (1996) *Nat. Struct. Biol. 3*, 224−227.
12. Bertrand, H.-O., Ha-Duong, T., Fermandjian, S., and Hartmann, B. (1998) *Nucleic Acids Res. 26*, 1261−1267.
13. Tisné, C., Simenel, C., Hantz, E., Schaeffer, F., and Delepierre, M. (1996) *Magn. Reson. Chem. 34*, s115−s124.
14. Piotto, M., Saudek, V., and Sklenar, V. (1992) *J. Biomol. NMR 2*, 661−665.
15. Baleja, J. D., Germann, M. W., van de Sande, J. H., and Sykes, B. D. (1990) *J. Mol. Biol. 215*, 411−428.
16. Sklenár, V., and Bax, A. (1987) *J. Am. Chem. Soc. 109*, 7525−7526.
17. Kupce, E., Boyd, J., and Campbell, I. D. (1995) *J. Magn. Reson. 106*, 300−303.
18. Lankhorst, P. P., Haasnoot, C. A. G., Erkelens, C., and Altona, C. (1984) *J. Biomol. Struct. Dyn. 1*, 1387−1405.
19. Lavery, R., Sklenar, H., Zakrzewska, K., and Pullman, B. (1986) *J. Biomol. Struct. Dyn. 3*, 989−1014.
20. Lavery, R., and Sklenar, H. (1988) *J. Biomol. Struct. Dyn. 6*, 63−91.
21. Mauffret, O., Hartmann, B., Convert, O., Lavery, R., and Fermandjian, S. (1992) *J. Mol. Biol. 227*, 852−875.
22. Lefebvre, A., Mauffret, O., Hartmann, B., Lescot, E., and Fermandjian, S. (1995) *Biochemistry 34*, 12019−12029.
23. Sodano, P., Hartmann, B., Rose, T., Wain-Hobson, S., and Delepierre, M. (1995) *Biochemistry 34*, 6900−6910.
24. Lavery, R., Parker, I., and Kendrick, J. (1986) *J. Biomol. Struct. Dyn. 4*, 443−461.
25. Weiner, S. J., Kollman, P. A., Case, D. A., Singh, U. C., Ghio, C., Alagona, G., Profeta, S. J., and Weiner, P. (1984) *J. Am. Chem. Soc. 106*, 765−784.
26. Cornell, W. D., Cieplak, P., Bayly, C. I., Gould, I. R., Merz, K. M. J., Ferguson, D. M., Spellmeyer, D. C., Fox, T., Caldwell, J. W., and Kollman, P. A. (1995) *J. Am. Chem. Soc. 117*, 5179−5197.
27. Flatters, D., Zakrzewska, K., and Lavery, R. (1997) *J. Comput. Chem. 18*, 1043−1055.
28. Lefebvre, A., Mauffret, O., Lescot, E., Hartmann, B., and Fermandjian, S. (1996) *Biochemistry 35*, 12560−12569.
29. Kim, S.-G., and Reid, B. R. (1992) *J. Magn. Reson. 100*, 382−390.
30. Clore, G. M., and Gronenborn, A. M. (1985) *FEBS Lett. 179*, 187−198.
31. Wüthrich, K. (1986) *NMR of proteins and nucleic acids*, John Wiley & Sons, New York.
32. van de Ven, F. J. M., and Hilbers, C. W. (1988) *Nucleic Acids Res. 16*, 5713−5720.
33. Wijmenga, S. S., Mooren, M. M. W., and Hilbers, C. W. (1993) in *NMR in macromolecules: a practical approach* (Roberts, G. C. K., Ed.) pp 217−288, Oxford University Press, New York.
34. Gorenstein, D. G., Schroeder, S. A., Fu, J. M., Metz, J. T., Roongta, V., and Jones, C. R. (1988) *Biochemistry 27*, 7223−7237.
35. Schroeder, S. A., Roongta, V., Fu, J. M., Jones, C. R., and Gorenstein, D. G. (1989) *Biochemistry 28*, 8292−8303.
36. Delepierre, M., Sodano, P., Gouyette, C., Namane, A., Igolen, J., and Virelizier, J.-L. (1996) *Magn. Reson. Chem. 34*, s67−s80.
37. Ott, J., and Eckstein, F. (1985) *Biochemistry 24*, 2530−2535.
38. El Antri, S., Mauffret, O., Monnot, M., Lescot, E., Convert, O., and Fermandjian, S. (1993) *J. Mol. Biol. 230*, 373−378.
39. Gorenstein, D. G. (1994) *Chem. Rev. 94*, 1315−1338.
40. Schneider, B., Neidle, S., and Berman, H. M. (1997) *Biopolymers 42*, 113−124.
41. Hartmann, B., Piazzola, D., and Lavery, R. (1993) *Nucleic Acids Res. 21*, 561−568.

42. Ulyanov, N. B., and Zhurkin, V. B. (1984) *J. Biomol. Struct. Dyn. 2*, 361−385.
43. Metzler, W. J., Wang, C., Kitchen, D. B., Levy, R. M., and Pardi, A. (1990) *J. Mol. Biol. 214*, 711−736.
44. Ulyanov, N. B., Gorin, A. A., Zhurkin, V. B., Chen, B.-C., Sarma, M. H., and Sarma, R. H. (1992) *Biochemistry 31*, 3918−3930.
45. Lefebvre, A., Fermandjian, S., and Hartmann, B. (1997) *Nucleic Acids Res. 25*, 3855−3862.
46. Sarma, R. H., Sarma, M. H., Dai, L., and Umenoto, K. (1997) *FEBS Lett. 418*, 76−82.

BI982402D